A study on the thermal resistance over solid-liquid-vapor interfaces in

a finite-space by a molecular dynamics method

C. S. Wang and J. S. Chen[*],

National Taipei University of Technology, Taiwan R.O.C.

1, Sec. 3, Chung-Hsiao E.Rd. Taipei 106, Taiwan

J. Shiomi and S. Maruyama

Department of Mechanical Engineering, The University of Tokyo,

7-3-1 Hongo, Bunkyo-ku, Tokyo 113-8656, Japan

*E-mail address: jongshun@ms70.url.com.tw,

TEL: 886-2-2771-2171 Ext. 2026, FAX: 886-2-2731-7191.

Abstract

Molecular dynamics of argon atoms in a nano-triangular channel which consists of

(111) platinum walls were studied. The molecular dynamics simulations aim to gain

understanding in the heat transfer through the channel including the influence of the

contact resistances which become important in small-scale systems. The heat transfer

properties of the finite-space system were measured at a quasi-steady non-equilibrium

state achieved by imposing a longitudinal temperature gradient to the channel. The results indicate that the total thermal resistance is characterized not only by the thermal boundary resistances of the solid-liquid interfaces but also by the thermal resistance in the interior region of the channel. The overall thermal resistance is determined by the balance of the thermal boundary resistances at the solid-liquid interfaces and the thermal resistance attributed to argon adsorption on the lateral walls. As a consequence, the overall thermal resistance was found to take a minimum value for a certain surface potential energy. A rich solid-liquid interface potential results in a reverse flow along the wall which gives rise to a stationary internal flow circulation. In this regime, the nanoscale-channel functions as a heat-pipe with a *real* steady state.

Nomenclature

k Spring constant

k_B Boltzmann constant

L_R Contact thermal thickness

M Mass flux

m Mass

N_a Number of atoms inside the adiabatic zone

Pt Platinum molecular

$q(Q)$ Heat flux

R^T System total thermal resistance

r Distance of Argon to Argon

T_c Control temperature (K)

T_{jump} Temperature jump

V Volume size

$<v_z>$ Average z-direction (axial direction) velocity

$v'z$ z-direction (axial direction) velocity fluctuation

$v_{z,i}$ z-direction (axial direction) velocity for ith atom

α Damping factor

ε Energy parameter of Lennard-Jones

λ Thermal conductions

ϕ Potential function

σ Length parameter of Lennard-Jones

σ_F Standard derivation of random exciting force

Sub/superscripts

V Channel interior

$cond$ Condensation zone

$evap$ Evaporation zone

int Pt and argon internal relation

Ar Argon

G Gas

L Liquid

I Intermediate

S Solid

$surf$ surface

W wall

1. Introduction

The study on the mechanisms of phase change behaviors in the solid-liquid and liquid-vapor interfaces is important, especially in micro-nanoscale systems. Since it is difficult to carry out experimental measurements in such small scales, molecular dynamics (MD) methods, being able to probe detailed pictures of the interfacial phenomena, have advantages in gaining fundamental understanding of the phase changes and their influence on the heat transfer [1]. The significant influence of the interfacial thermal resistance between two phases has been extensively discussed in the literature [2-9].

Maruyama and Kimura [2] directly measured the thermal boundary resistance over a solid-liquid interface using non-equilibrium MD simulations. The system consists of two parallel solid walls between which argon atoms are confined, where liquid argon (Ar) is in contact with the walls and the saturated vapor Ar occupies the bulk region. The simulations modeled nanoscale gap between two-dimensional solid-liquid interfaces by adopting the periodic boundary conditions in the wall-parallel directions. A quasi-steady state was achieved by controlling the walls at different temperature and the temperature jumps at the solid-liquid interfaces were measured. It was demonstrated

that the thermal resistance could not be neglected for small-scale systems and interfacial thermal resistance was equivalent to the resistance of 5~20 nm thick liquid layer and was strongly dependent on the wettability. The dependence of the thermal boundary resistance on the wettability was also pointed out by Xue *et al.* [3] using a non-equlibrium MD simulation. They identified two regimes with different trends of the thermal boundary resistance with respect to the strength of the solid-liquid interactions.

Matsumoto [4] investigated the thermal resistance of several types of interfaces of a Lennard-Jones FCC crystal using molecular dynamics simulations, and found that a temperature gaps exist at the interfaces even with absence of lattice defects or mismatches. Due to the temperature discontinuity, the thermal energy flux is smaller than that through a single crystal without the interfaces.

Ohara and Suzuki [5], by means of non-equilibrium MD simulations, examined the heat transfer at the solid-liquid interface in terms of the intermolecular energy transfer, a concept developed based on detailed studies of heat conduction in the bulk liquid phase water [6] and Lennard-Jones fluid [7]. They found that the reduction of the macroscopic heat flux can be attributed to the intermolecular energy transferred against the macroscopic heat flux at the interface. Lee *et al.* [8] addressed that when the system size was in the microscopic scale as in thin film composites, the small thermal resistance due

to the molecular level ordering became noticeable even for preferred solid-solid contacts.

Based on the knowledge and methodologies from the above studies, in the current paper, we study the influence of the interfacial thermal resistance in more complex system; a nanoscale heat pipe where the interface of the lateral adiabatic walls (Fig. 1) gives an additional essence to the overall heat transfer. Such influence of lateral wall is of significant importance on thermal devices in practical situations. Although there have been a number of studies devoted to the interfacial thermal resistance in nanoscale, to the best of our knowledge, there is yet no work on heat transfer in a nano-heat-pipe. Unlike the case with the two-dimensional interface with the periodic boundary conditions, where most of the atoms in the mid-gap region are found in the vapor phase with relatively minute thermal resistance [2], with the presence of the lateral wall, some atoms are adsorbed on the lateral walls and induce local thermal resistance hence change the averaged thermal resistance in the intermediate zone. This thermal resistance gives rise to a unique trend of the overall heat transfer characteristics. In the current paper, we compute the overall heat transfer of a heat pipe flow for various wettability properties of the walls. The paper demonstrates the existence of the minimum overall thermal resistance for optimal wall wettability.

2. Molecular dynamics methods

Figure 1 shows the configuration of a 9.36×8.11×21.96 nm and θ=60° triangular nanopipe which consists of fixed platinum (Pt) lateral single layer surfaces and capped with three phantom layers [2] of solid Pt at top and bottom ends. Liquid Ar accumulates at the top (condensation zone) and bottom (evaporation zone) surfaces, whereas the saturated Ar vapor accumulates in the middle zone. The Ar-Ar interactive force is expressed by the Lennard-Jones potential of the form:

$$\phi(r) = 4\varepsilon\left[\left(\frac{\sigma}{r}\right)^{12} - \left(\frac{\sigma}{r}\right)^{6}\right],\tag{1}$$

which uses the cut off distance 3.5σ and the corresponding parameters σ_{Ar}=0.34 nm, m_{Ar}=6.036×10-26 kg and ε_{Ar}=1.67×10-21 J. The phantom layers with an fcc(111) crystal structure have 1156 Pt atoms on each layer. The Pt phantom atoms oscillate with the harmonic potential with parameters, m_{Pt}=3.24×10-24 kg, σ_{s}=0.28 nm (equilibrium distance) and k=46.8 N/m (spring constant). It should be noted that the effects due to free electron transfer in the solid walls are ignored. The potential function between horizontal solid walls (Fig. 2) and Ar atoms was also expressed by Lennard-Jones potential function with length parameter σ_{int} =(σ_{s}+σ_{Ar})/2=0.309 nm and the energy

parameter ε_{int}. The interaction potential between argon atoms and the lateral wall, which consists of three solid Pt layers, was represented by one-dimensional integrated potential functions [9]. By integrating the Lennard-Jones potential function over one layer fcc(111) surface we obtain,

$$\Phi(l) = \frac{4\pi\sqrt{3}}{15} \frac{\varepsilon_{int}}{\sigma_s^2} \left[2 \left(\frac{\sigma_{int}}{l} \right)^{10} - 5 \left(\frac{\sigma_{int}}{l} \right)^{4} \right], \qquad (2)$$

where l is the coordinate normal to the surface. While full integration of uniform solid atoms [10] is often used for representation of solid walls, in the current study, we adopted the layer-by-layer integration for better representation of the potential field near the surface. The second and third layers can be taken into account by adding the functions based on l locations of the corresponding layers. The minimum ε_{surf} of the function in Eq. (2) appears when $l=\sigma_{int}$ as,

$$\varepsilon_{surf} = \frac{4\pi\sqrt{3}}{5} \left(\frac{\sigma_{int}}{\sigma_s} \right) \varepsilon_{int}. \qquad (3)$$

The value of ε_{int} was varied between 0.527×10^{-21} J to 1.169×10^{-21} J denoted as E2~E6 inheriting the notations from Maruyama and Kimura [2] in order to highlight the difference.

Temperature of the horizontal solid walls was controlled by placing a layer of "phantom" atoms beneath the layer of *real* solid surface [2]. The phantom atoms model

an infinitely thick solid wall kept at a constant temperature T_c with proper heat conduction characteristics [11]. A phantom molecule is connected to each molecule of the surface solid layer with a spring of $2k$ in the vertical direction and springs of $0.5k$ in two horizontal directions. In addition, phantom molecule was connected to the fixed frame with a spring of $2k$ and a damper of $\alpha = m\omega_D\pi/6$ in the vertical direction and with springs of $3.5k$ and dampers of α in two horizontal directions. Here, ω_D is the Debye frequency. Each phantom molecule is excited by the random force of Gaussian distribution with the standard deviation $\sigma_F = \sqrt{\dfrac{2\alpha k_B T_c}{\Delta t}}$. The energy flux to the system can be accurately calculated by integrating the exciting force and the damping force applied to phantom molecules [2].

In this paper, the damping constant α=5.184×10^{-12} kg/s, Boltzmann constant k_B=1.381×10^{-23} and time step Δt=5 fs. The isothermal temperature T_c was set at 100 K on the top wall and 120 K on the bottom wall.

Initially, 5472 Ar atoms are conformably arranged with equal distance (σ_{Ar}) inside the triangular pipe and then Ar atoms are kept at 110 K with auxiliary velocity scaling control for 500 ps. Meanwhile, the temperature of the Pt phantom walls is also maintained at 110 K. At t=500 ps, the temperature control is turned off until 1000 ps to equilibrate the system. After t=1000 ps, the phantom wall temperatures are set at 100 K

(condensation) and 120 K (evaporation) to impose the temperature gradient. Compared with the previous case with absence of side walls [2], the presence of the lateral walls gives an additional complication to the picture of energy flux in the interior volume of channel as indicated in Fig. 2 with q_V^G, q_V^L and q_V^I. Especially, as it will be shown later, the non-trivial Pt-Ar surface potential energy can cause a reverse flow along the walls.

The energy transport in the interior volume Q_V can be quantified in connection with the following general energy flux, [12-14]

$$Q = \frac{1}{2V}\left[\sum_{i=1}^{N} m_i v_i^2 v_i + \sum_{i=1}^{N}\sum_{j\neq i}^{N} \phi_{ij} v_i - \sum_{i=1}^{N}\sum_{j\neq i}^{N} \left(\bar{r}_{ij} \cdot \bar{f}_{ij} \right) v_i \right] \tag{4}$$

The first term is the kinetic energy, the second term the potential contribution and the last term the pressure work. In the gas phase, the expression can be reduced to the mean kinetic energy and the fluctuating kinetic energy as,

$$Q_V^G = \frac{3\langle v_z \rangle N_V k_B T}{2V} + \frac{1}{V}\sum_{i=1}^{N} E_i v'_{z,i} \tag{5}$$

where $E_i = \frac{1}{2}mv_i^2$.

The overall energy flux through the adiabatic region can be computed as,

$$Q_V^T = Q_V^G + Q_V^L + Q_V^I. \tag{6}$$

3. Results and Discussions

Figure 3(a) depicts the time histories of spatially averaged temperature of the two controlled end-walls (T_w^{evap}=120 K and T_w^{cond}=100 K) and Ar atoms [Fig. 3(b)]. By initially equilibrating the system by isothermal boundary condition at 110K, the Ar temperature reaches equilibrium before t=1000 ps. After applying the temperature difference at the end-walls (t=1000 ps), the system goes through transient relaxation phase of about 10 ps before it approaches the quasi-steady state as seen in the convergence of the time history of the liquid Ar temperature. As in Maruyama and Kimura [2], the time window of quasi-steady state was determined by the time-independence of the temperature profile and energy budget on the phantom walls. It was confirmed that a quasi-steady temperature field could be achieved after a transient duration of 10 ps after imposing the temperature gradient. The energy fluxes added and subtracted from the system by the phantom controllers were calculated within the duration of the quasi-steady state and the values are denoted in Table 1. For instance, for case E4, the averaging was carried out from 2000 ps to 4000 ps and the computed energy fluxes at evaporation and condensation sides were q_w^{evap}=47.33 MW/m^2 and q_w^{cond}=58.67 MW/m^2, respectively. Due to the similarity of the two values of heat flux

on top and bottom walls, the current system can be regarded to be in a quasi-steady state, where constant heat flux through the system is driving a steady temperature distribution [2].

Figure 3(b) exhibits the time history of number of Ar atoms in the three zones; evaporation, intermediate (middle) and condensation zones (Fig 2) for the case E4. While nearly time-invariant saturated vapor Ar exists in the middle zone, number of atoms N in both top and bottom liquid zones increased and decreased at constant rates. Now the phase-change rate dN/dt of top and bottom liquid zones can be calculated to be 408/ps (condensation) and -368/ps (evaporation), respectively. Such quasi-steady state with constant flow rate can be achieved for all the tested cases, where the detailed data of other cases (E2~E6) are presented in Table 1.

Figure 4 denotes the number density profile and the temperature profile along the flow direction for case E4. The data are averaged temporally for 100 ps and spatially over the x-y section. Figure 4(a) denotes the density distribution at around 2000, 3500 and 5000 ps. The figure provides the streamwise profile of the phase change whose overall evolution has been depicted in Fig. 3(b). It can be observed that the density gradient remains almost constant during the quasi-stationary transport. The sharper fluctuations of the density distribution near the solid walls exhibit the layering

structures due to the walls whose intensity depends on the wettability. Figure 4(b)

depicts the temperature profile averaged over a time duration of 2000 ps (t=2000-4000

ps) which exhibits discontinuous jumps of ΔT^{evap}=4.66 K and ΔT^{cond}=5.48 K at top

and bottom walls, respectively. The thermal resistance $R=\Delta T/q_w$ can be now computed

as $R_{contact}^{Evap}=0.124\times10^{-6}$ m^{2}K/W and $R_{contact}^{cond}=0.145\times10^{-6}$ m^{2}K/W. The streamwise

temperature profile in the interior of the pipe exhibits constant temperature gradients of

three regions (evaporation, middle and condensation). By knowing the temperature

gradient in addition to the heat flux through the system, the thermal conductivity of each

region can be computed through the Fourier's law, $q_w = \lambda\left(\partial T \big/ \partial z\right)$. The thermal

conductivity λ_L of liquid Ar on top and bottom ends for case E4 were computed to be

λ_L^{evap}=0.086 W/mK and λ_L^{cond}=0.083 W/mK. In order to interpret the physical meaning

of the contact thermal resistance, an effective thickness of the thermal resistance

$L_R = \lambda_L R$ is calculated. As shown in Table 1, the values of L_R for all the tested cases are

consistent with those of Maruyama and Kimura [2], which are in the range of 5~20 nm.

Figure 5 (a) shows the molecular distribution with different surface potential. It

reveals that the interfaces between liquid Ar on both ends and vapor Ar have convex

shapes in cases E2 and E3, whereas they have concave shapes in cases E5 and E6. This

means that the adhesion force (Pt-Ar) is smaller than the attractive force (Ar-Ar) for the

former cases, and vice versa for the latter cases. The two groups of cases are divided by the intermediate case of E4 with a flat interface. In Fig. 5(b), the number density contours of Ar are shown for cases E2, E4 and E6. The number density contours are displayed for x-y planes in different z-locations corresponding to condensation, middle and evaporation zones at 3000 ps. The figures are to provide the pipe cross sectional view of the inhomogeneous Ar distribution observed in Fig. 5(a). The figures show a strong tendency of Ar aggregation in the channel grooves due to the rich local surface potential. Now we are able to observe that the concave interface in Fig 5(a) has a triangle distribution in cross sectional plane. Note that the ratio of Ar density at evaporation and condensation side is different among three cases since the mass transport ratio is case dependent [Fig.3 (b)]. As for the adiabatic zone, while case E4 shows that the aggregation of Ar is mainly in the grooves, case E6 exhibits a considerable Ar concentration on the lateral walls.

As shown in Fig. 5, due to the presence of lateral walls, Ar takes different phases depending on the intensity of the influence from the walls. In order to clarify the characteristics of mass transport under different wall effects and corresponding phase changes, we divide the system into three regions in terms of the potential ϕ,

$$\phi_g \equiv \sum \phi_{ij} \geq -2 \times 10^{-21} J \qquad \text{(Gaseous regime)},$$

$$\phi_l \equiv \sum \phi_{ij} \leq -10 \times 10^{-21} J \qquad \text{(Liquid regime)},$$

$$-2 \times 10^{-21} J > \phi_i > -10 \times 10^{-21} J \quad \text{(Intermediate regime)}.$$

Although the criteria may not strictly reflect the phase change limits, the separation is useful to visualize the distribution of atoms under various wall effects. Gaseous Ar atoms (white) far from the side walls, liquid Ar atoms (green) due to Ar adsorption on walls and the interfacial region of the intermediate phase (orange). Fig. 6 shows the axial velocity profiles of the three regions for cases E2, E4 and E6 at 3000 ± 100 ps. The velocities of gaseous and intermediate regions were case-dependent, i.e. depended on the surface energy, but were positive for all the cases. On increasing the surface energy (ε_{int}), the velocity in the intermediate region is reduced and the range of vapor region with finite velocity is expanded from 10 to 20 nm. Furthermore, the value of ε_{int} has significant impact on the velocity of the liquid Ar region. For relatively small values of ε_{int} such as E2 [Fig. 6(a)] and E3, the velocity is nearly zero in the entire liquid region. In these cases, as shown in Fig. 5, the lateral walls have minor influence to the mass transport hence two liquid Ar drops are merely formed on top and bottom ends due to cohesion. On the contrary, for relatively larger values of ε_{int} such as in cases E5 and E6 [Fig. 6(c)], the liquid velocity becomes negative (backward steaming) and the liquid atoms flow from the top to the bottom along the lateral walls. The over-saturated liquid

at the condenser is driven reversely to compensate the dry-out of the evaporator i.e. the local density drop at the evaporator is felt globally in the system.

Note that this is unique to a small-scale system and different from macro-scale heat pipes where the return flow is caused by gravity. Compared with the transient quasi-steady heat transport with one-way mass transport, the return flow would certainly be a source of thermal resistance and holds a significant impact to the overall thermal resistance in the nano-scale system. As for the case E4 with intermediate ε_{int}, as shown in Fig. 6(b), Ar atoms in all the phases experience transport in the positive z-direction, i.e. there is contribution to the heat transfer rate from all the phases in the middle zone. Consequently, comparing the mass flow rates M of E2~E6 cases in Table 1, it can be observed that E3 and E4 have larger values than the others. The maximum value of M=678.4 kg/m^{2}s was obtained for case E4.

The influence of ε_{int} on the heat flux and thermal resistance of the middle zone calculated by Eq. (4, 5) is summarized in Fig. 7. The figure clearly indicates the existence of three regimes of ε_{int} with different characteristics of heat flux. Firstly, there is the regime A where Q_V^T energy flux increases with ε_{int}. In this regime, the phenomenon is reduced to two liquid drops with vapor gap and the heat flux is mainly governed by the evaporation speed of the hot liquid. Since the heat transport from the

phantom walls to the interacting Ar atoms increase with ε_{int}, or the interfacial thermal resistance decreases with ε_{int}, the evaporation rate of argon increases with ε_{int}. The variation of the heat flux in this regime, however, has minute effect on the thermal resistance. Further increase of ε_{int} triggers a distinct influence of the lateral walls, which results in reduction of the heat flux Q_V^T (regime B). The reduction of Q_V^T accelerates with increasing ε_{int} and eventually drives the reverse flow of the liquid Ar along the wall (regime C) as the over-saturated argon is converted back towards the evaporation zone. The reduction of the heat transport due to the lateral-wall effect is reflected in the trend of the thermal resistance, $R_V = \Delta T_V / Q_V^T$, in the interior region which rapidly increases with ε_{int}.

Fig. 8 shows the dependence of total thermal resistance on the surface potential ε_{int}. The total thermal resistance is,

$$R^T = R_V + R_{contact}^{evap} + R_{contact}^{cond}. \qquad (7)$$

The values of $R_{contact}^{evap}$ and $R_{contact}^{cond}$ were found to be identical to the values computed by Maruyama and Kimura [2] for two-dimensional interfaces, independently of the cases (E2-E6). As denoted in Fig. 8, $R_{contact}^{evap}$ and $R_{contact}^{cond}$ exhibit nearly monotonous decrease with increasing ε_{int} due to the strengthening of the interaction between liquid Ar and phantom layers. The unique aspect of the present work in comparison with the

previous work [2] is the presence of the thermal resistance of the middle region and its dependence on ε_{int} as discussed earlier for Fig. 7. This gives rise to the minimum R^T for ε_{int} corresponding to case E4 as shown in Fig. 8. This case represents, if we were to promote heat transfer of the system, the case with the optimal balance of the thermal boundary resistance at Ar-phantoms interface and balance and the absorption of argon inside the channel groove and lateral Pt walls due to the non-trivial surface potential effect. For this particular nanopipe, the highest mass-flow rate was calculated to be 678.4 Kg/m^{2}s.

It should be noted that, the negative liquid flow along the lateral wall is preferable in practical applications of heat pipes as it return the liquid to the evaporator and prevent the dry-out. This particularly important in nano systems where the body force from the gravity is small.

4. Conclusions

A quasi-steady non-equilibrium molecular dynamics simulation was performed to investigate the overall thermal resistance in a nanoscale triangular heat pipe filled with argon. The temperature control was applied to heat and cool the bottom and top walls

where evaporation and condensation of argon take place, respectively. On the contrary to the commonly studied system with two-dimensional interfaces with the periodic boundary conditions, in the current system with presence of lateral walls, the middle zone between the evaporation and condensation zones plays an important role on characterizing the overall thermal resistance. The influence of the walls on the heat and mass transport depends on the surface potential ε_{int}. In small ε_{int} regime, the lateral walls play a minor role and the system can be reduced to the evaporating and condensing droplets on bottom and top end walls. In this regime, the heat transfer is dominantly characterized by the thermal boundary resistance at the solid-liquid interface, hence the total thermal resistance R^T decreases with ε_{int}. On the other hand, in large ε_{int} regime, the distinct absorption of Ar atoms on the pipe-walls gives rise to a distinct thermal resistance in the middle zone. By further increasing ε_{int}, the lateral-wall effect eventually results in the reverse flow of oversaturated liquid argon from the condensation zone along the lateral walls mainly in the grooves of the nanopipe. At the crossover of the two ε_{int} regimes the total thermal resistance R^T takes a minimum value. The results demonstrate the existence of an optimal wall-wettability for best heat transfer through the heat pipe. For the current system, the minimum value of R^T was calculated to be 2.3×10^{-7} m^{2}K/W at a flow rate of 678.4 kg/m^{2}s for $\varepsilon_{int}=0.848 \times 10^{-21}$ J. Furthermore,

when the nano-channel functions as a heat pipe with the steady flow circulation (in regime C), even though R^T is off the above stated minimum value, it is still considerably less than the value of a macro-scale heat pipe, even with the loop heat pipe [15], is $R=2\sim4\times10^{-3}$ m^{2}K/W. On considering the practical applications as heat pipes, the negative liquid flow along the lateral wall is preferable as it returns the liquid to the evaporator and prevents the dry-out, which is of particular importance in nano systems where the gravitational body force is small.

Acknowledgements

References

[1] Maruyama S., Molecular Dynamics Method for Micro/Nano Systems, Handbook of Numerical Heat Transfer (2006), 659-695.

[2] Maruyama S., Kimura T., A study on Thermal Resistance over a Solid-Liquid Interface by the Molecular Dynamics Method, Therm. Sci. Eng. 7 (1999) 1.

[3] Xue L., Keblinski P., Phillpot S. R., Eastman J. A., Two Regimes of Thermal Resistance at the Liquid-Solid Interface, J. Chem. Phys. 118 (2003) 337.

[4] Matsumoto M., Wakabayashi H. and Makino T. Thermal Resistance of Crystal Interface: Molecular Dynamics simulation, Heat Transfer-Asian Research 34 (2005) 135-146.

[5] Ohara T., Suzuki D., Intermolecular Energy Transfer at a Solid-Liquid Interface, Micro. Thermophys. Eng. 4 (2000) 189-196.

[6] Ohara T., Intermolecular Energy Transfer in Liquid Water and Its Contribution to Heat Conduction: An Molecular Dynamics Study, J. Chem. Phys. 111 (1999) 6492-6500.

[7] Ohara T., Contribution of intermolecular energy transfer to heat conduction in a simple liquid, J. Chem. Phys. 111 (1999) 9667-9672.

[8] Matamis M. G., Cahill D. G.., Allen W. P., Thin-Film Materials and Minimum Thermal Conductivity, Microscale Thermphys. Eng. l2 (1998) 31-36.

[9] Maruyama S., Kurashige. T., Matsumoto S., Yamaguchi Y., and Kimura T., Liquid Droplet in Contact with A Solid Surface, Microscale Thermphys. Eng. 2 (1998) 49-62.

[10] Allen M. P., Tildesley D. J., Computer Simulation of Liquids, Oxford University Press. Oxford. 1987

[11] Tully J. C., Dynamics of Gas-Surface Interactions: 3D Generalized Langevin Model Applied to fcc and bcc Surfaces, J. Chem. Phys. 73 (1980) 1975-1985.

[12] Kotake S., Wakuri S., Molecular Dynamics Study of Heat Conduction in Solid Materials, JSME Int. J., Series B. 37 (1994) 103-108.

[13] Hafskjold B., Ikeshoji T., On the Molecular Dynamics Mechanism of Thermal Diffusion in Liquid, Molecular Phys. 80 (1993) 1389-1412.

[14] Ikeshoj T., Hafskjold B., Non-Equilibrium Molecular Dynamics Calculations of Heat Conduction in Liquid and through Liquid-Gas Interface, Molecular Phys. 81 (1994) 251-261.

[15] Maydanik F., Vershinin V., Miniature Loop Heat Pipes- A Promising Means for Cooling Electronics, IEEE Transactions on Components and Packaging Technologies 28 (2005) 290-296.

Figure captions

Fig. 1   The configuration of nanoscale triangular heat transfer system; (a) the cross-section of argon atoms confined in the triangular pipe with lateral Pt walls indicated by dashed lines, (b) the stereogram, where the blue (dark) atoms denote horizontal solid Pt layers. The lateral walls are indicated with dashed lines.

Fig. 2   Schematics of heat transfer of the system with evaporator on the left and condenser on the right. Gas, liquid and solid regions are colored with white, light blue and dark blue, respectively. Temperature jumps (T_{JUMP}) due to the contact thermal resistances at the solid-liquid interfaces are indicated together with the thermal resistance thicknesses.

Fig. 3   (a) Time histories of the temperature of Ar atoms and the solid walls (case E4). (b) Time histories of the number of Ar atoms in evaporation, middle and condensation regions (case E4). After equilibrating the system, temperature control was turned on at t=1000 ps.

Fig. 4   (a) Density distributions of Ar atoms in the z-direction and its time evolution (case E4). (b) Axial temperature profile of the system (case E4).

Fig. 5　(a) Side views of the molecular distribution in the triangular pipe. (b) Top views of the molecular distribution in the cross sections at various z-locations corresponding to condensation, middle and evaporation regions. The data are averaged for a time duration of $t=3000\pm100$ ps.

Fig. 6　The axial velocity profiles of Ar in three different regimes of potential energy; $\phi_l \leq -10\times10^{-21}J$, $-10\times10^{-21}J > \phi_i > -2\times10^{-21}J$ and $\phi_g \geq -2\times10^{-21}J$ roughly denoting the liquid, intermediate and gas Ar atoms, respectively. The figures indicate the dependence of the velocity profile and direction on the surface energy.

Fig. 7　The surface energy ε_{int} dependence of the heat fluxes and thermal resistance in the pipe interior. The total interior heat flux Q_V^T consists of heat fluxes of Ar atoms in gas phase Q_V^V, intermediate phase Q_V^I and liquid phase Q_V^L.

Fig. 8　Variation of the thermal resistances with respect to the surface energy ε_{int}. The total thermal resistance R^T consists of thermal resistance of the interior R_V, evaporator R_W^e and condenser R_W^c.

Table caption

Table 1 Simulation conditions and calculated values.

3 solid layers (Pt)

Liquid (Ar)

Vapor (Ar)

Intermediate (Ar)

Liquid (Ar)

3 solid layers (Pt)

Vlz

c

a

b

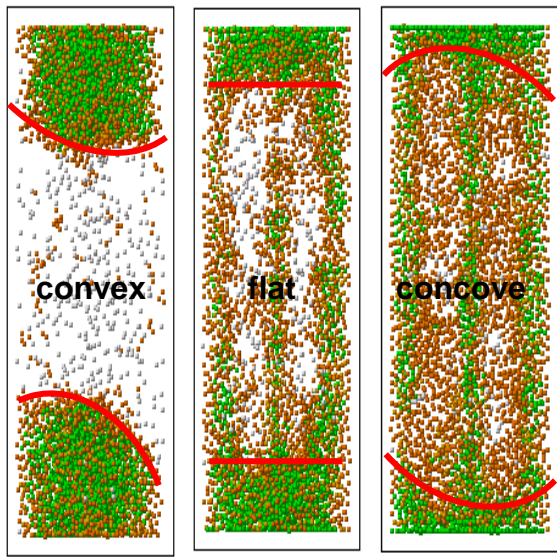Vly

Vlx
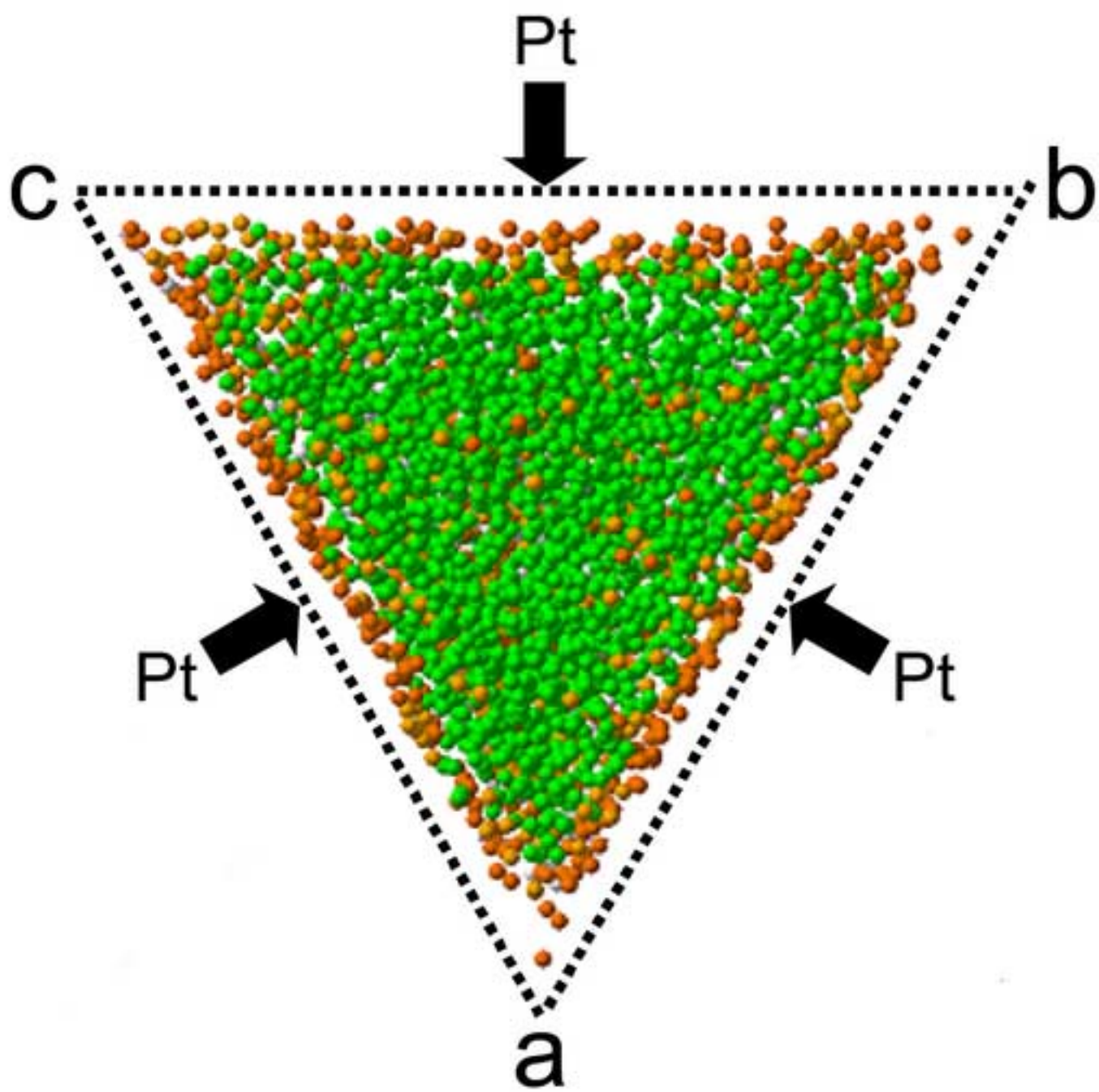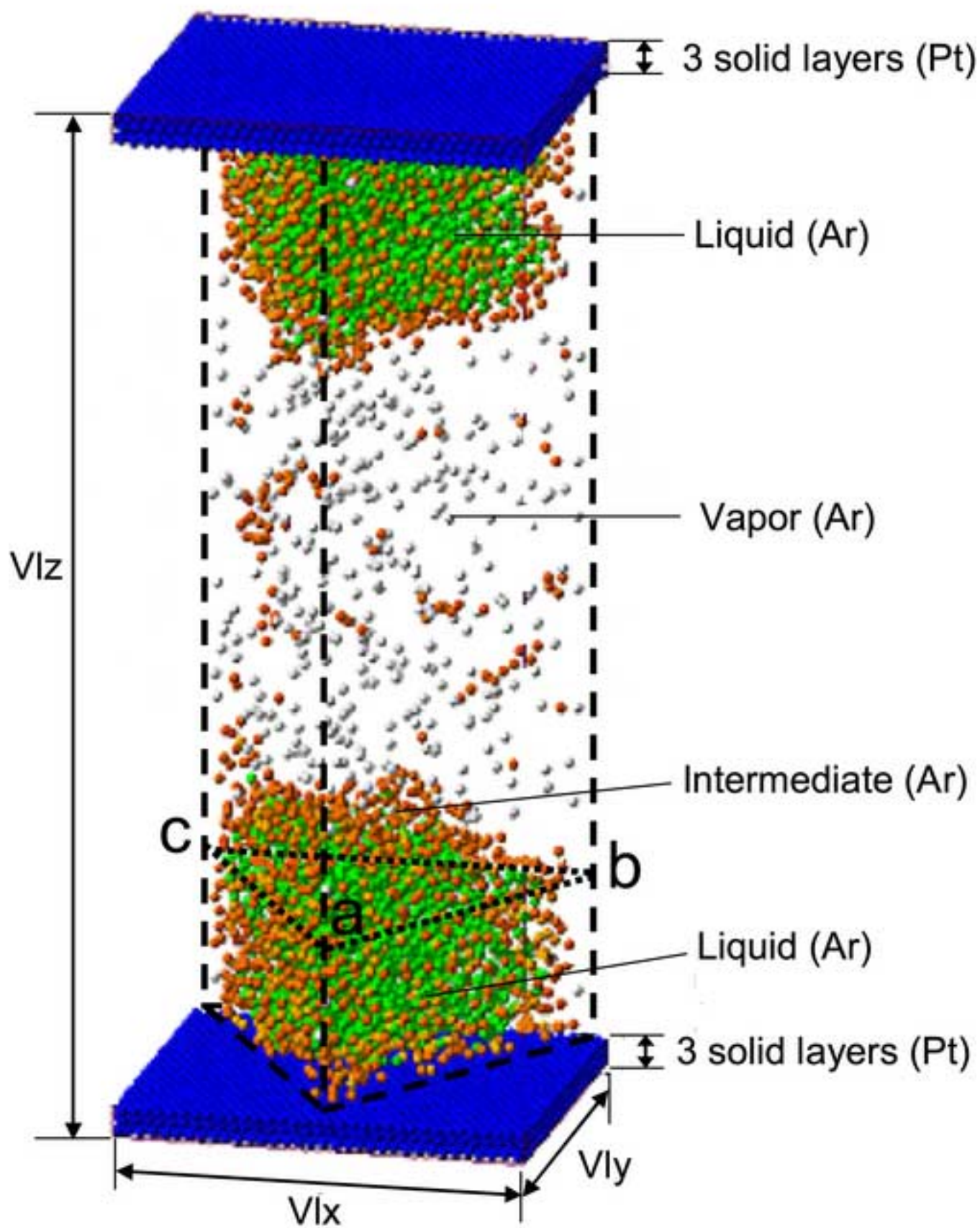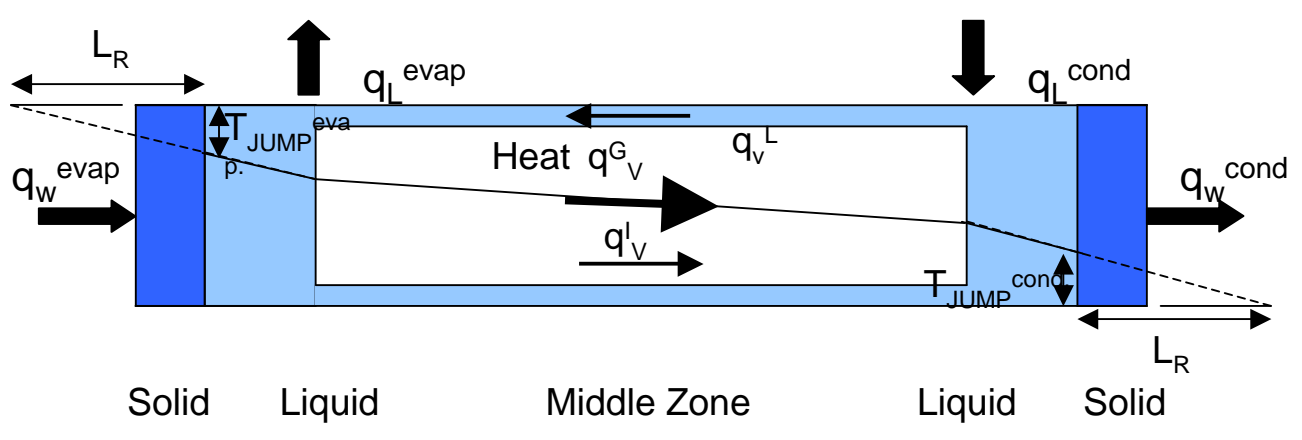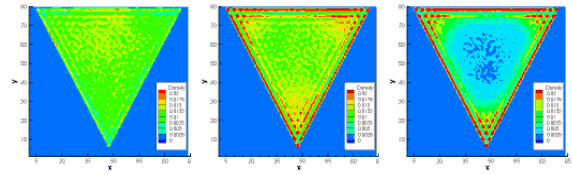
Figure2

Figure3

Figure4
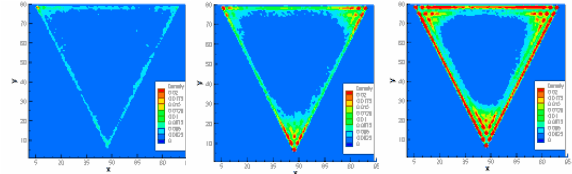
Figure5

convex
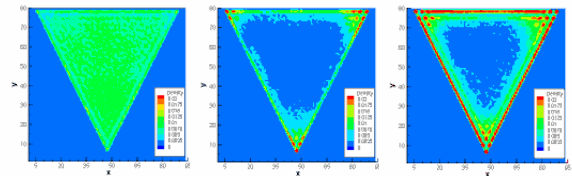
flat

concove
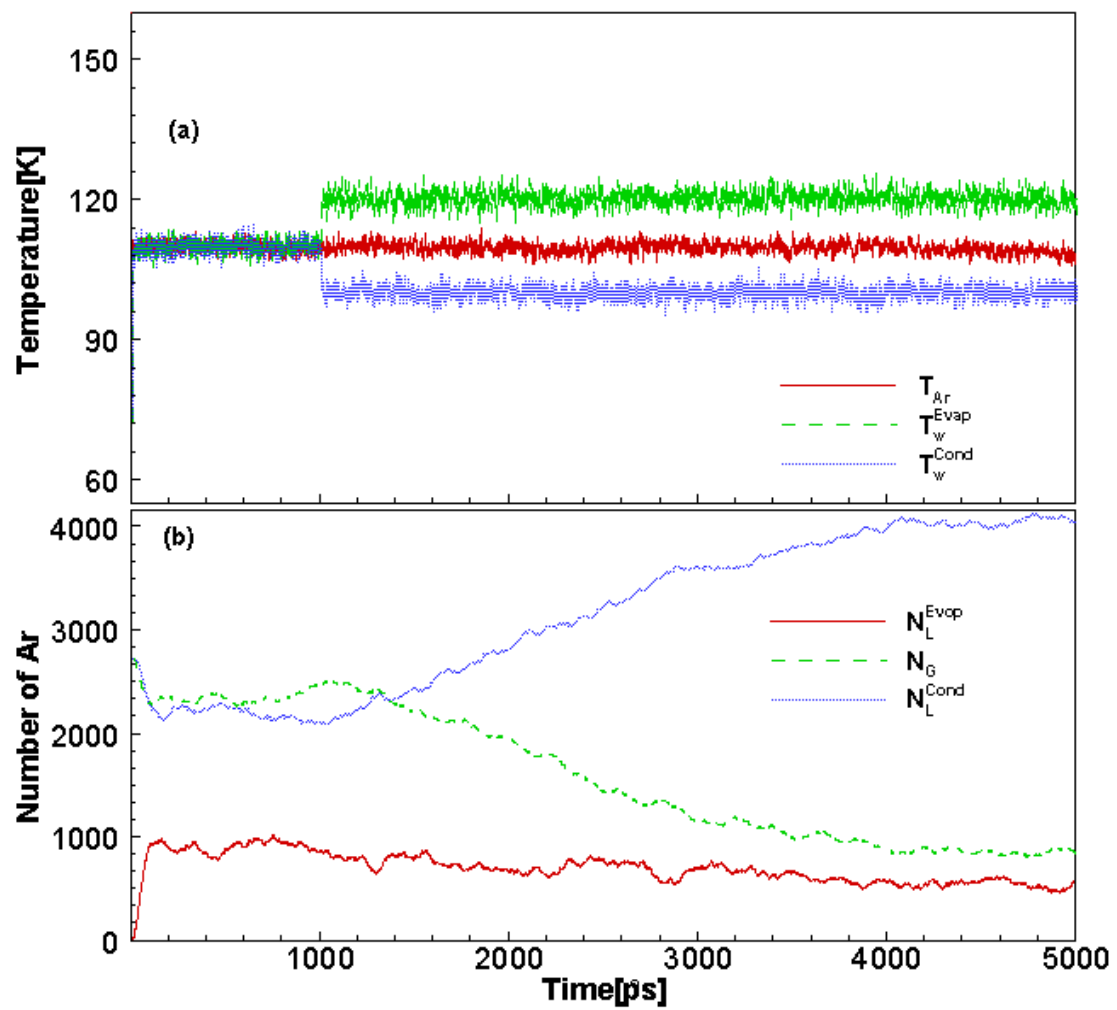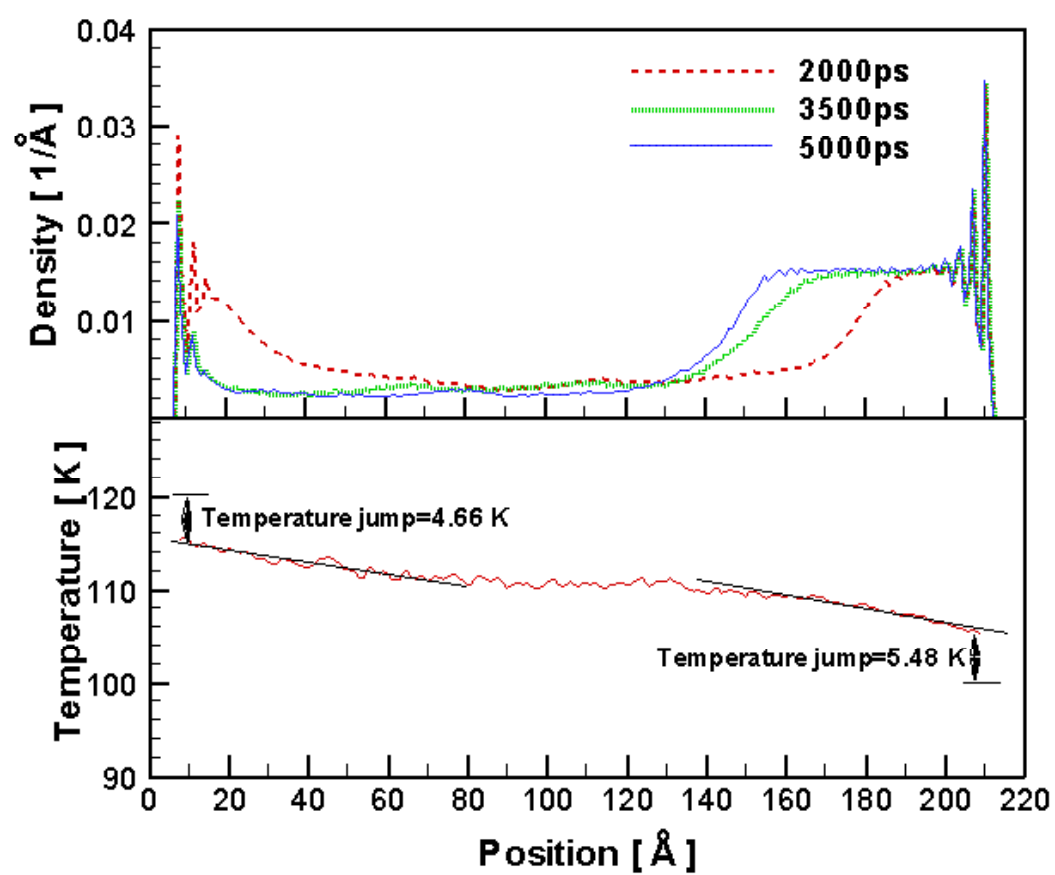
E2   E4   E6

(a)

Cond.

Inter.

Evap.

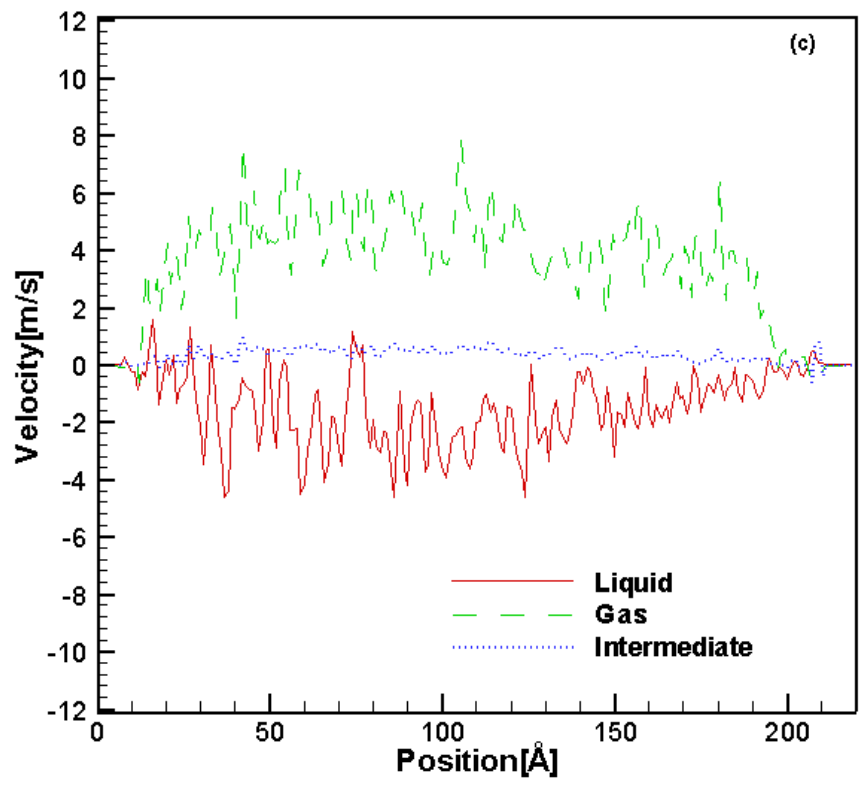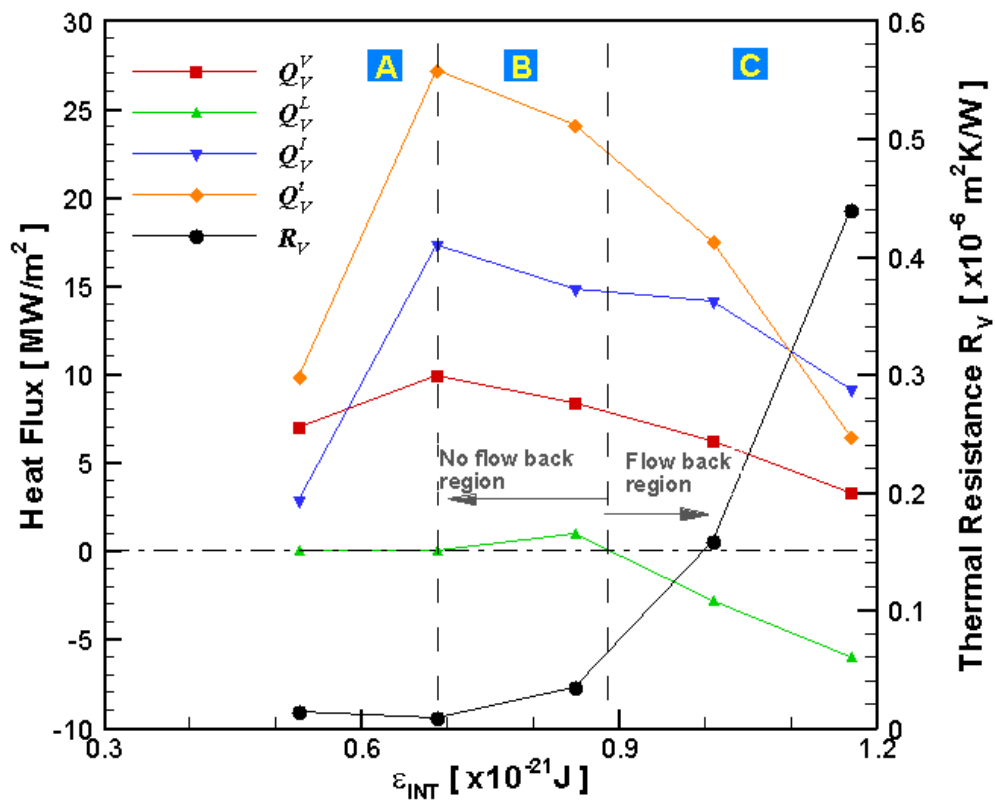E2   E4   E6

(b)

Figure6

Figure7

Figure8

Table
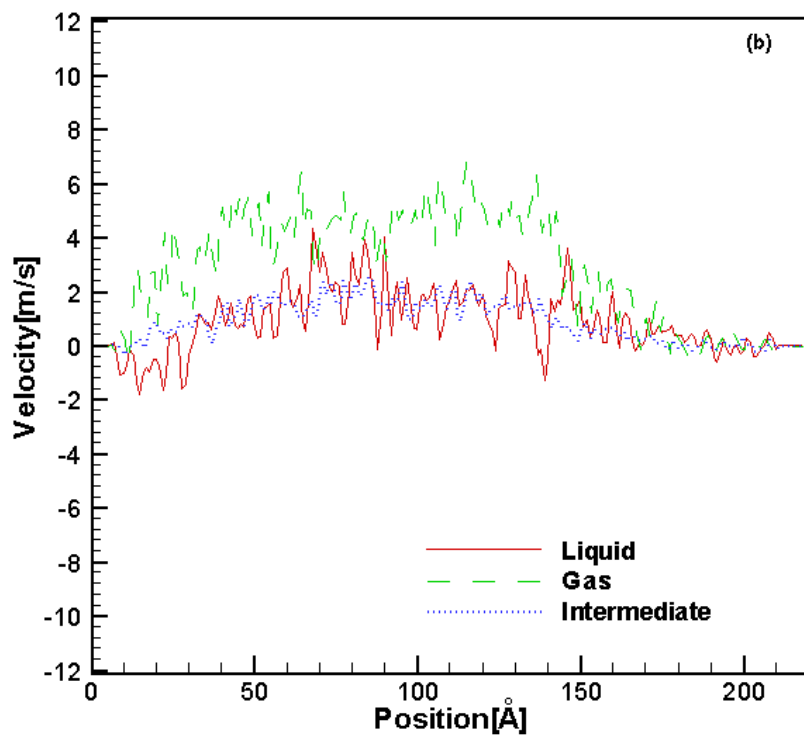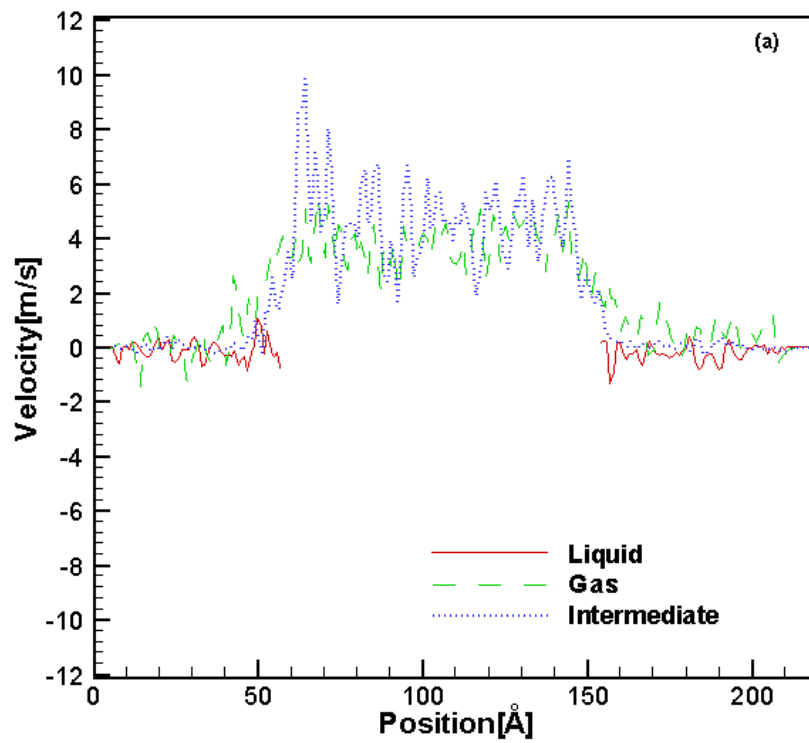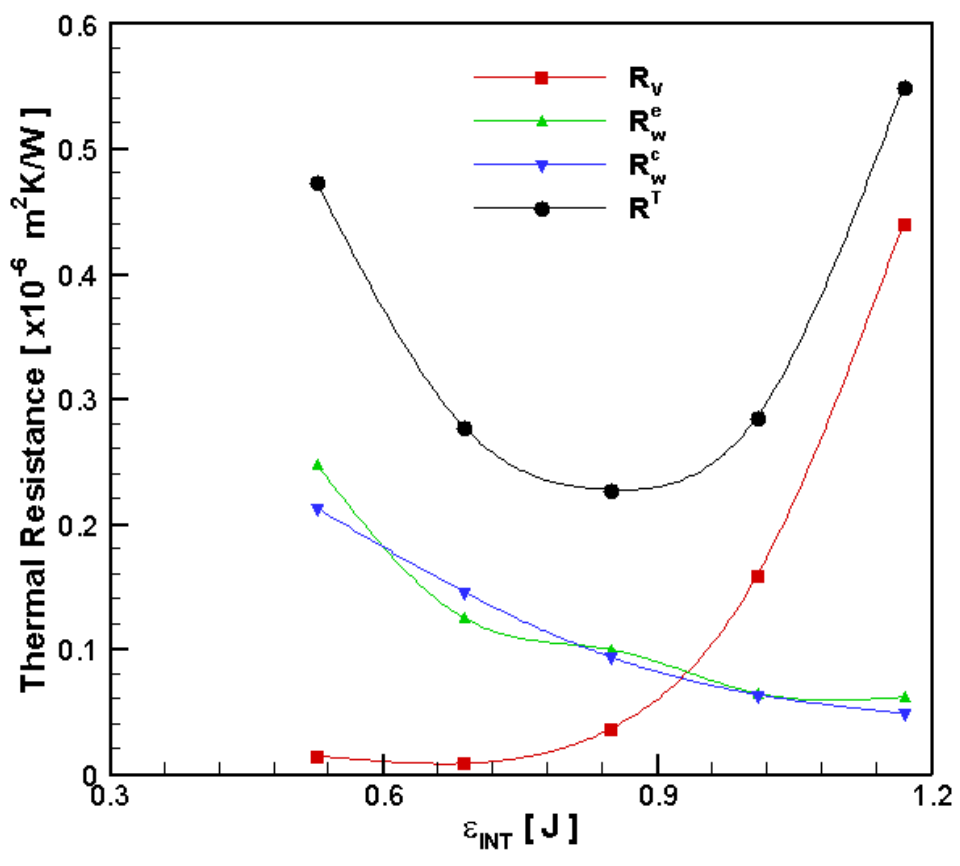
Label		ε_{int} ($\times 10^{-21}$ J)	Q_w (MW/m^2)	T_{jump} (K)	R_T ($\times 10^{-6}$ m^{2}K/W)	λ_L (W/mK)	L_R (nm)	dN_L/dt (1/ns)	M (kg/m$^2 \cdot$ s)
E2	evap.	0.527	32.33	7.99	0.247	0.087	21.5	-152.3	273.4
	cond.		36.33	7.69	0.212	0.120	18.4	160.7	
E3	evap.	0.688	45.17	5.59	0.124	0.164	10.8	-327.0	560.8
	cond.		46.33	6.71	0.145	0.045	12.6	315.0	
E4	evap.	0.848	47.33	4.66	0.099	0.086	8.6	-368.3	678.4
	cond.		58.67	5.48	0.093	0.083	8.1	408.3	
E5	evap.	1.009	49.33	3.17	0.064	0.064	5.6	-82.7	176.7
	cond.		56.00	3.53	0.063	0.088	5.5	119.7	
E6	evap.	1.169	52.00	3.19	0.061	0.074	5.3	-17.0	52.4
	cond.		48.67	2.33	0.048	0.059	4.2	43.0	